


Article

Creep Behavior of Diffusion-Welded Alloy 617

Injin Sah ^{1,*} , Jong-Bae Hwang ² and Eung-Seon Kim ¹

¹ Next-Generation Fuel Technology Development Division, Korea Atomic Energy Research Institute, Daejeon 34057, Korea; kimes@kaeri.re.kr

² Department of Materials Science and Engineering, Chungnam National University, Daejeon 34134, Korea; hwangjb@kaeri.re.kr

* Correspondence: injin@kaeri.re.kr; Tel.: +82-42-866-6264

Abstract: Plate-type heat exchangers are anticipated to be used in the next-generation nuclear industry, and solid-state diffusion welding is a critical technology for building plate-type heat exchangers with high integrity. In this study, we manufactured a diffusion weldment and evaluated its creep behavior. Microscopic analysis revealed that Al-rich oxides were developed along the interface, significantly impeding grain-boundary movement across the interface. Oxide-containing planar grain boundaries resulted in premature brittle fracture at the interface with less than 9% creep strain under all test conditions. The time to rupture and time to 1% creep strain of the diffusion weldment were less than those of the as-received alloy, while the slopes in double-logarithmic plots were almost identical for both alloys. In a Larson–Miller parameter study, the stress to rupture of the diffusion weldment reached 95.59% of that of the as-received alloy, whereas the stress to 1% creep strain steeply decreased in the low-stress range.

Keywords: Alloy 617; diffusion welding; stress-rupture; creep; Larson–Miller



Citation: Sah, I.; Hwang, J.-B.; Kim, E.-S. Creep Behavior of Diffusion-Welded Alloy 617. *Metals* **2021**, *11*, 830. <https://doi.org/10.3390/met11050830>

Academic Editors: Elisabetta Gariboldi and Jiri Svoboda

Received: 12 April 2021

Accepted: 17 May 2021

Published: 19 May 2021

Publisher's Note: MDPI stays neutral with regard to jurisdictional claims in published maps and institutional affiliations.



Copyright: © 2021 by the authors. Licensee MDPI, Basel, Switzerland. This article is an open access article distributed under the terms and conditions of the Creative Commons Attribution (CC BY) license (<https://creativecommons.org/licenses/by/4.0/>).

1. Introduction

Plate-type heat exchangers have attracted much attention for application in the next-generation nuclear industry because they can realize high heat-transfer efficiency between primary and secondary systems [1–3]. Solid-state joining methods, such as brazing, transient liquid phase bonding, and diffusion welding, are essential processes for manufacturing such plate-type heat exchangers.

Brazing [4–10] and transient liquid phase bonding [11–29] are attractive for joining Ni-based superalloys. For example, Luo et al. used a BNi-2 filler metal to join Hastelloy C-276 (UNS N10276) [7]. Jalilian et al. studied the influence of the process parameters (filler metal thickness and holding time for isothermal solidification) of transient liquid phase bonded Inconel 617 (UNS N06617) using BNi-3 (Ni-4.5Si-3B) [12] and BNi-6 (Ni-10P) [19]. Kapoor et al. successfully attained a high-temperature (750 °C) yield strength of approximately 86% of that of as-received Haynes 230 (UNS N06230) in their transient liquid phase bonding experiment [27]. Farzadi et al. used BNi-1 (Ni-13Cr-4.5Si-4.2Fe-2.8B-0.06C) and BNi-2 (Ni-7Cr-4.5Si-4.5Fe-3.2B-0.06C) as filler metals and performed microscopic analysis, microhardness tests, and shear-strength tests [29].

In brazing and transient liquid phase bonding, a homogenization heat treatment may result in microstructure and mechanical properties similar to those of as-received alloy. However, secondary brittle intermetallic phases are inevitably created near the interface because of the presence of melting-point depressants, such as boron, phosphorous, and/or silicon, in an interlayer. Such secondary phases degrade mechanical properties with negligible permanent deformation at the interface.

Diffusion welding without the application of interlayers seems to be an alternative solution [30–39]. The following are representative examples of diffusion welding for Ni-based superalloys. Zhang et al. explored the influence of bonding temperature, time,

and pressure on joint quality [30]; they achieved a tensile strength comparable to that of the parent metal at room temperature. Shirzadi and Wallach proposed a fascinating method to remove surface oxides that inhibit metal-to-metal joints of superalloys [31]. Ravisankar et al. proposed the use of a grain-growth equation and Pilling's model, which was originally developed to predict the rate of void closure, on the diffusion welding of SU 263 (UNS N07263) [33]. Basuki et al. systematically optimized the diffusion-welding process (applied compression stress, bonding duration, and surface roughness) of Hastelloy C-22 (UNS N06002) [34]; they attained a tensile strength comparable to that of the as-received alloy, but the toughness of the diffusion weldment remained poor owing to the evolution of Mo-rich carbide and Mg-rich oxide at the interface. Mizia et al. attempted to evaluate the usefulness of thermodynamic and diffusion computation tools for optimizing the diffusion-welding parameters for Alloy 800H (UNS N08810) [35]. Sah et al. reported the effect of post-weld heat treatment on the recovery of tensile ductility of diffusion-welded Alloy 617 and Haynes 230 (UNS N06230) [36]. Song et al. evaluated the bonding performance by measuring the thermal/mechanical properties and conducting pressure-resistance tests [37]. Xiong et al. reported a comprehensive review of the mechanical properties and their corresponding microstructural features [38]. Recently, Sah et al. provided reasonable evidence for grain-boundary movement at the interface [39]; they emphasized the control of micro-chemistry at or near the surface to be bonded to obtain a precipitate-free interface. In most cases, owing to the evolution of secondary precipitates at the interface, the mechanical performance of diffusion weldment was lower than expected.

Research has been actively progressing to build small modular-type nuclear power plants; in turn, codification work for plate-type heat exchangers for use in the nuclear industry has attracted significant interest [40–43]. As plate-type heat exchangers are designed to operate at high temperatures for a long time, such high-temperature components must possess good oxidation/corrosion resistance, phase stability, and superior mechanical properties. The most significant factor affecting the structural integrity is a time-dependent mechanical property called creep. However, many studies on solid-state joining were biased toward the characterization of microstructural features, phase identification, hardness measurement across the interface, and observation of room-temperature tensile behavior. As mentioned above, the degradation of mechanical properties at room and high temperatures is unavoidable. However, very few researchers have conducted high-temperature mechanical tests [1,39,44–49], and joint features, such as the extent of degradation in mechanical properties compared to the as-received alloy, have not been reported to date.

The objective of the present study is to evaluate the creep behavior of diffusion-welded Alloy 617. Interface microstructural analysis is introduced on the basis of the authors' previous work. Further, the creep behavior is elucidated using the results of stress-rupture experiments conducted at high temperatures. In addition, a time-temperature parameter for the life estimation of the diffusion weldment is presented. Finally, the predicted values for the diffusion weldment are compared with those for the as-received alloy.

2. Materials and Methods

We used Alloy 617 (Ni-Cr-Co-Mo), which is a solid-solution-strengthened Ni-based superalloy that retains superior mechanical properties and oxidation/corrosion resistance at high temperatures. A sheet with dimensions of 3048 (L) mm × 1219 (W) mm × 1.60 (T) mm was supplied by the Special Metals Company. Table 1 presents the chemical composition of the sheet (Heat No. XX4516UK), which meets the ASTM: B168-19 specification. This alloy contains Cr and Al for oxidation/corrosion resistance as well as Co and Mo for solid-solution hardening. It is widely known that the grain boundary of this alloy is slightly covered with Cr-rich $M_{23}C_6$ carbide, and Ti-rich MC carbide is evenly spread in the matrix.

Table 1. Chemical composition of the Alloy 617 sheet in wt. %.

Element	Ni	Cr	Co	Mo	Fe	Mn	Al
ASTM: B168-19 Sheet	44.5 min 52.9	20.0–24.0 22.6	10.0–15.0 11.5	8.0–10.0 9.6	3.0 max. 1.28	1.0 max. 0.15	0.8–1.5 1.23
Element	C	Cu	Si	S	Ti	B	P
ASTM: B168-19 Sheet	0.05–0.15 0.09	0.5 max. 0.03	1.0 max. 0.11	0.015 max. 0.001	0.6 max. 0.35	0.006 max. 0.004	N/A 0.003

The supplied sheet was sectioned using the water-jet cutting method. Sixty sheets with dimensions of 200 (L) mm \times 200 (W) mm \times 1.60 (T) mm were prepared for diffusion welding. The rolling direction of the sheet was not considered. The number and dimensions of the sheets employed in this study were determined on the basis of the procedure and performance qualification listed in Section IX QW-185 of the American Society of Mechanical Engineers (ASME). Both sides of all sheets were mechanically ground with up to #1200 SiC grit paper to remove surface contamination, ultrasonically cleaned, and then dried in the air before being placed into diffusion-welding equipment.

Diffusion welding was conducted at 1150 °C for 2 h (4 h in total, including homogenization of the temperature in the diffusion-welding equipment) with a compressive uniaxial pressure of 14.7 MPa. A high vacuum condition ($\sim 10^{-6}$ Torr) was employed to impede the formation of tenacious oxides on the surface as much as possible. The filler metal was not applied to preserve the similarity of joints. The stack was subjected to post-weld heat treatment (PWHT) at 1150 °C for 8 h in a high-vacuum ($\sim 10^{-6}$ Torr) furnace for further atomic diffusion near the interfaces. The stack was cooled to room temperature using inert high-purity nitrogen gas. These parameters produced a stack (hereinafter, diffusion weldment) with dimensions of 200 (L) mm \times 200 (W) mm \times 91.05 (T) mm.

For scanning electron microscopy (SEM) analysis, mechanically sectioned specimens were dipped into a chemical etchant ($\text{HNO}_3\text{:HCl} = 1\text{:}3$, vol.%) for approximately 40 s to reveal the grain boundary and interface of the diffusion weldment. The focused ion beam (FIB; FEI NOVA200) method was used to extract a specimen at an interface for transmission electron microscopy (TEM; JEM-ARM200F, JEOL Ltd., Tokyo, Japan) analysis.

Cylindrical bar-type specimens with a gauge diameter of 6.0 mm and a gauge length of 30.0 mm were produced for stress-rupture tests (Figure 1), which were conducted at high temperatures of 800, 850, 900, and 950 °C according to the ASTM: E139-11 (2018) standard. Interfaces in the direction perpendicular to tensile loading were located in the gauge section. The distance between interfaces approximately corresponds to the thickness of the sheet (~ 1.60 mm). The circular ridges were machined at both ends of the gauge section to attach an extensometer.

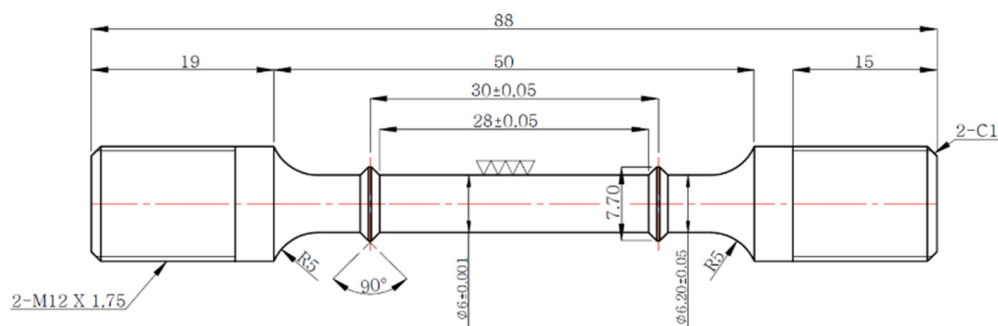
**Figure 1.** The dimension of specimens for the stress-rupture test (in mm).

Figure 2 shows the test apparatuses for the stress-rupture test. Both dead weight and lever type machines were employed in this study; a lever arm ratio of 20:1 was applied. The creep strain was determined by the elongation measured by the extensometer equipped at the circular ridges. Relative movement of the circular ridges during the stress-rupture test was displayed in a linear variable differential transducer (LVDT) attached at the bottom side of the furnace, and then the record was automatically transferred to a personal computer. A three-zone split furnace was used. A K-type thermocouple was used to monitor the temperature in the gauge section. The temperature was maintained within ± 2 °C during the stress-rupture test. We produced the pull rod and jig with Ni-based superalloy to prevent severe oxidation and thermal degradation.

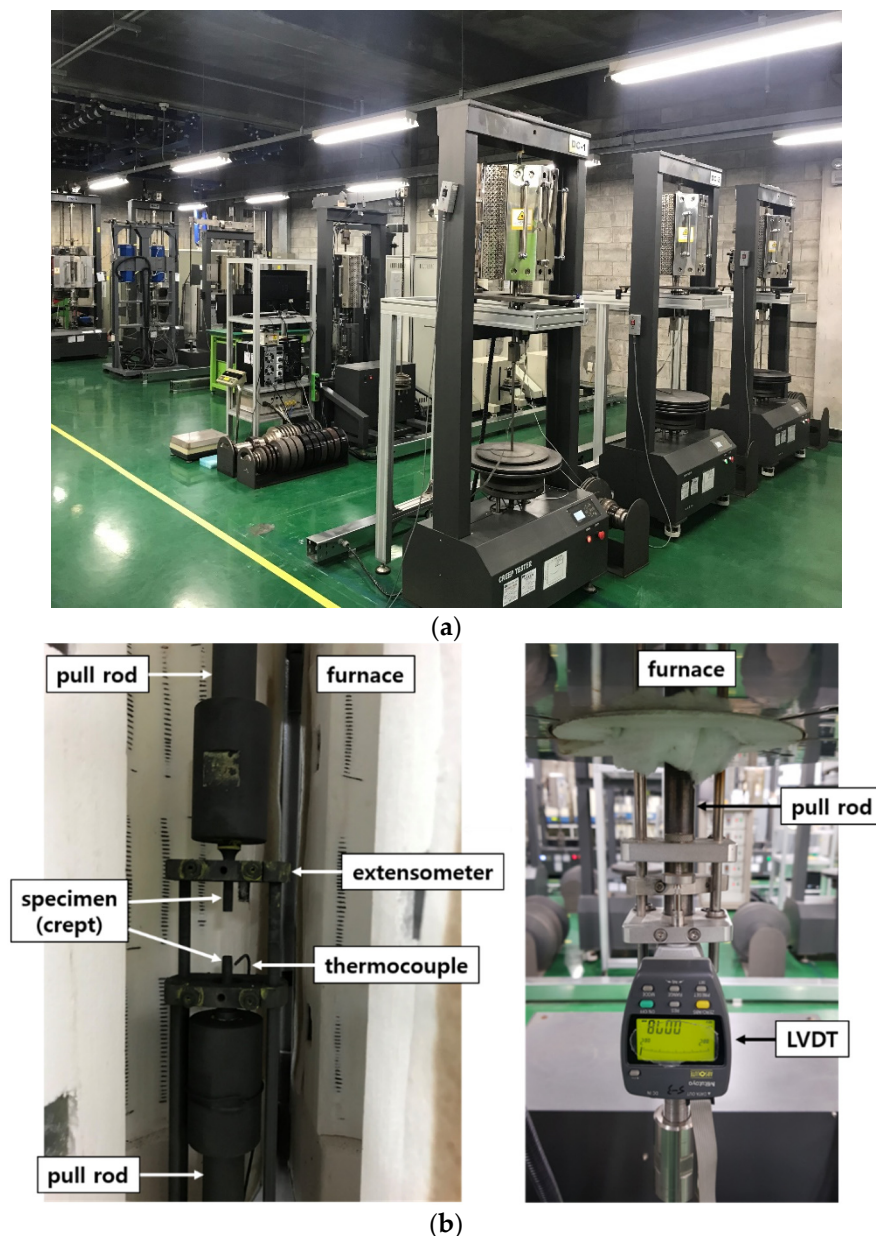


Figure 2. (a) Test apparatuses for the stress-rupture test and (b) elongation-measuring system.

3. Results and Discussion

3.1. Microstructure

Figure 3 shows cross-sectional SEM and TEM micrographs of the region near an interface. No defects (detectable cracks, incomplete bonds, or porosity) were observed

near the interface (an interface is marked with arrows in each micrograph), implying that the diffusion-welding parameter used in this study is applicable to this alloy. Further, the interface can be easily recognized. Secondary precipitates are observed along the interface, and simultaneously, grain-boundary movement across the interface is limited.

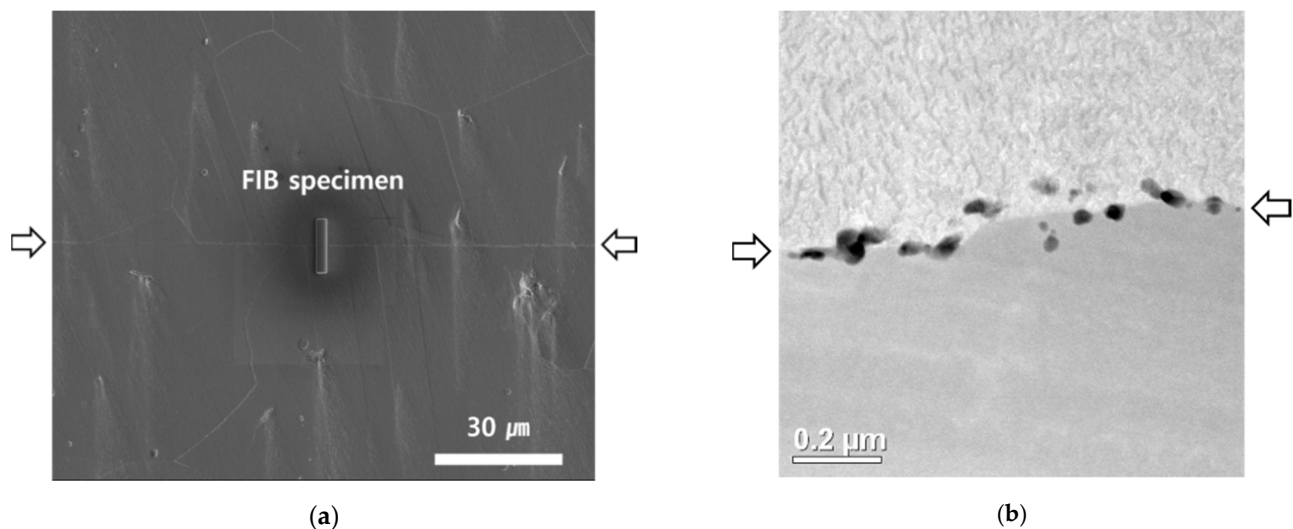


Figure 3. Electron microscopy analysis of the diffusion-welded Alloy 617 near the interface: (a) SEM and (b) TEM. The arrows indicate the interface of the diffusion weldment. (a) shows the location for FIB specimen extraction.

Following the authors' previous TEM analysis using energy-dispersive X-ray spectroscopy (EDS) and electron energy-loss spectroscopy (EELS), the secondary precipitates formed along the interface were identified as Cr-rich carbides and Al-rich oxides [36,39]; as indicated in the authors' previous work, the black dots in Figure 3b are Al-rich oxides. The Al-rich oxides stem from the reaction between Al in the matrix and oxygen in the diffusion-welding equipment. Although the diffusion-welding process was conducted under a high-vacuum condition ($\sim 10^{-6}$ Torr), the oxygen level in the diffusion-welding equipment was high enough to produce Al-rich oxides on the surfaces at high temperatures. The discrete Al-rich oxides along the interface restricted grain-boundary movement, leaving a planar grain boundary. Some researchers have emphasized that the evolution of stable surface oxides (film or discrete type) is a governing factor limiting metal-to-metal joining [34,36,38,39,50–54].

3.2. Creep Behavior

Stress-rupture tests were conducted at 800, 850, 900, and 950 °C in ambient air under various stress levels to characterize the creep behavior of the diffusion weldment. A fixed load was applied to the specimen in each stress-rupture test. The stress levels and test temperatures applied in this study reflect the anticipated operating conditions of high-temperature reactor systems [55].

Figure 4 shows curves of creep strain versus time, where Figure 4a–d shows the results of stress-rupture tests performed at 800, 850, 900, and 950 °C, respectively. Table 2 summarizes the time to rupture (t_{rup}), strain at rupture (ϵ_{rup}), and time to 1% creep strain ($t_{1\%}$).

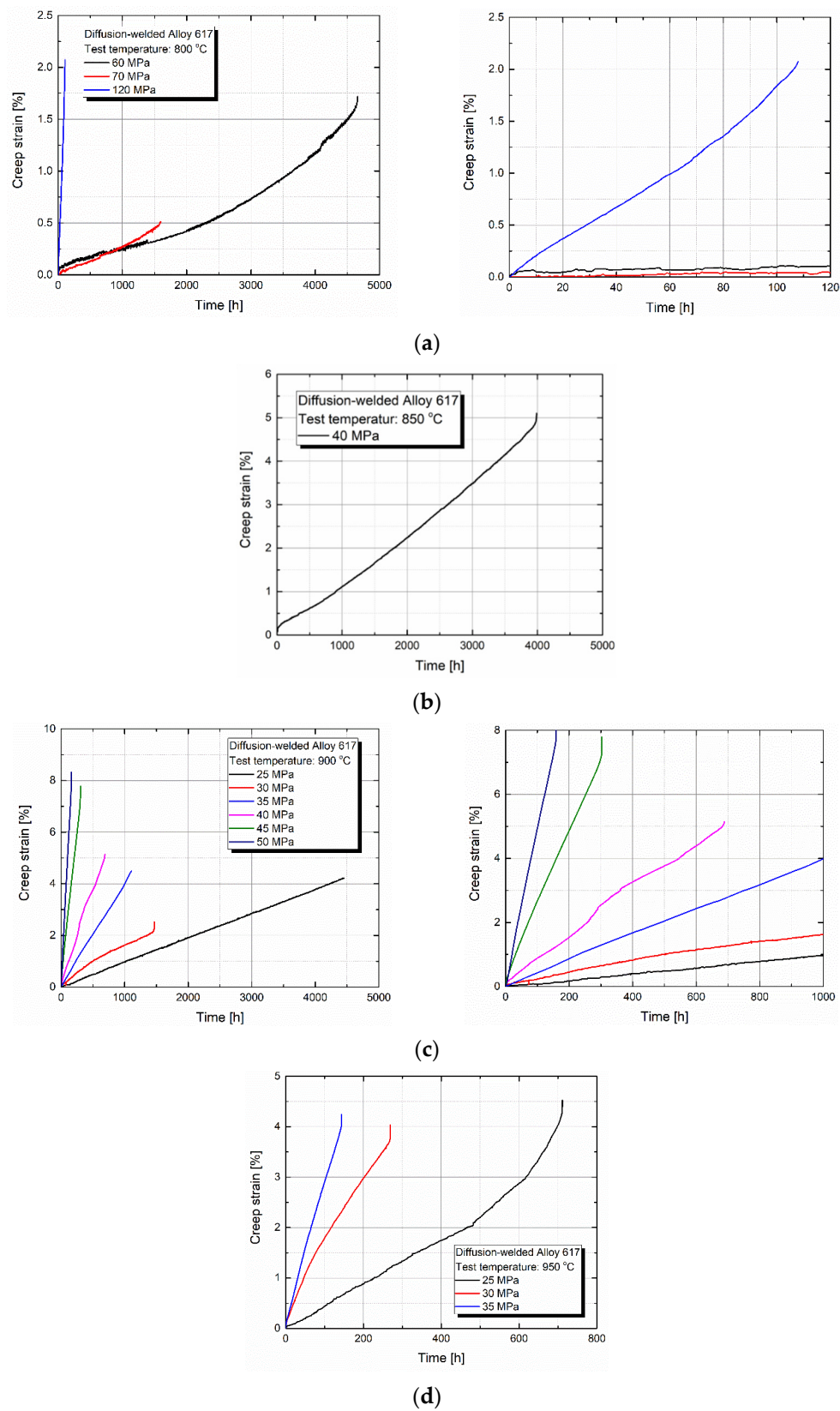


Figure 4. The curves of the creep strain versus time of the diffusion-welded Alloy 617. A stress-rupture test was conducted at: (a) 800 °C, (b) 850 °C, (c) 900 °C, and (d) 950 °C.

Table 2. The stress-rupture test data showing t_{rup} , ϵ_{rup} , and $t_{1\%}$.

Temperature (°C)	Stress (MPa)	t_{rup} (h)	ϵ_{rup} (%)	$t_{1\%}$ (h)	Remark
800	60	4661	1.71	3647.1	-
	70	4596	0.51	-	-
	100	546	-	-	N/A
	120	107	2.07	60.9	-
850	40	3985	5.10	898.9	-
	50	1327	4.71	-	N/A
900	25	4454	4.22	1017.9	-
	30	1466	2.52	490.7	-
	35	1107	4.49	239.1	-
	40	688	5.13	119.6	-
	45	303	7.78	31.1	-
	50	159	8.32	20.2	-
950	20	2308	-	-	N/A
	25	711	4.52	227.1	-
	30	269	4.04	46.9	-
	35	143.6	4.24	31.2	-

At 800 °C, creep curves were drawn for applied stresses of 60, 70, and 120 MPa (Figure 4a). A test conducted at 100 MPa showed abnormal features in the creep curve, which could be attributed to the jig material; hence, the data for 100 MPa were discarded (Table 2). Further, a creep curve with $t_{rup} = 4661$ h was successfully obtained for applied stress of 60 MPa. Primary and secondary creep stages were rarely observed. The tertiary creep stage commenced early at a low creep strain. At this temperature, the strains at rupture were low (<2.07%). At 850 °C, one creep curve was drawn for applied stress of 40 MPa (Figure 4b). In this case, t_{rup} was 3985 h, and ϵ_{rup} was 5.10%. Again, primary and secondary creep stages were hardly observed. The specimen was fractured in the tertiary creep stage but showed little permanent deformation. The creep curves at 900 °C are shown in Figure 4c. In this case, t_{rup} and ϵ_{rup} were 4454 h/4.22%, 1466 h/2.52%, 1107 h/4.49%, 688 h/5.13%, 303 h/7.78%, and 159 h/8.32% under stresses of 25, 30, 35, 40, 45, and 50 MPa, respectively. Surprisingly, the diffusion weldment spends most of the time in the secondary creep stage at this temperature and does not enter the tertiary creep stage. This is an indication of immediate fracture during the course of gradual creep crack propagation in the secondary creep stage. Figure 4d shows the creep curves at 950 °C. In this case, t_{rup} and ϵ_{rup} of the specimens were 711 h/4.52%, 269 h/4.04%, and 143.6 h/4.24% at stresses of 25, 30, and 35 MPa, respectively. At this test temperature, the secondary creep stage was dominant at high-stress levels (30 and 35 MPa), whereas the tertiary creep stage, in addition to the secondary creep stage, was observed at a low-stress level (25 MPa).

It is well known that as-received Alloy 617 specimens are fractured in the ductile mode in short-term (high-stress level) tests, and the fracture mode changes to brittle in long-term (low-stress level) tests. Further, ϵ_{rup} usually decreases as t_{rup} increases. In contrast, the ϵ_{rup} of the diffusion weldment did not exhibit a clear relation with t_{rup} . In all cases, limited creep strains (<9%) with fractures near the interface were observed in the diffusion weldment.

Figure 5a,b shows plots of log stress versus log time to rupture and log stress versus log time to 1% creep strain, respectively. Both plots clearly show linearity, implying that the following power-law function is applicable for the diffusion weldment:

$$\sigma = A \cdot t^m, \quad (1)$$

where σ is the stress (MPa), A (MPa·h^{-m}) is a material constant, and m is an exponent. A is the intercept, and m is the slope in the double-logarithmic plot. Here, t can be the time to rupture, time to tertiary creep stage (t_{ter}), or time to 1% creep strain. In this study, we

plotted the time to rupture and time to 1% creep strain because the time to tertiary creep stage was not ascertained in some of the stress-rupture tests (Figure 4).

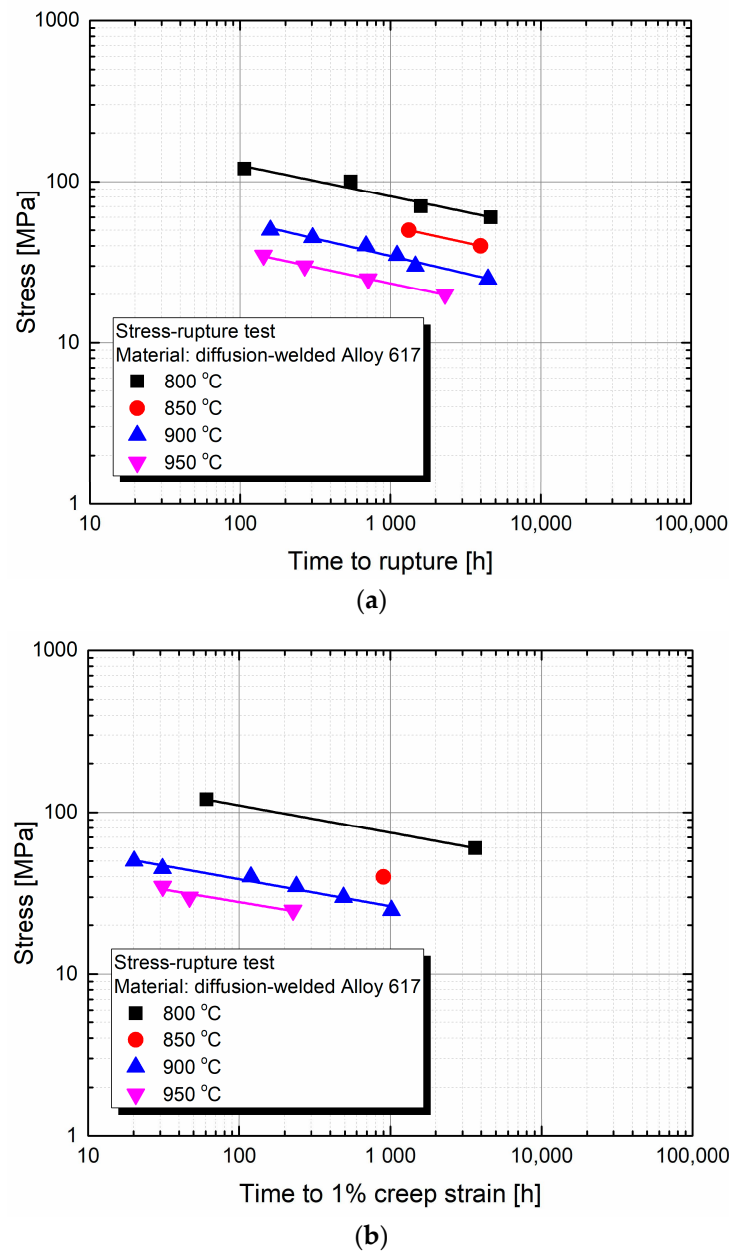


Figure 5. Double-logarithmic plots of stress versus time: (a) log stress versus log time to rupture and (b) log stress versus log time to 1% creep strain.

The values calculated using Equation (1) are listed in Table 3. The intercept of the double-logarithmic plot for the time to rupture (A_{rup}) increased from 92.46 MPa·h^{−m} at 950 °C to 307.70 MPa·h^{−m} at 800 °C. Similarly, the intercept of the double-logarithmic plot for the time to 1% creep strain ($A_{1\%}$) increased from 57.18 MPa·h^{−m} at 950 °C to 240.68 MPa·h^{−m} at 800 °C.

The absolute inverse of the slope ($|1/m|$) is usually considered an indicator of the creep deformation and fracture mechanism. The absolute inverse values of the slope of the double-logarithmic plot for the time to rupture ($|1/m_{rup}|$) were in the range of 4.639–5.172. A value of ~5 is typical in pure metals and Class I solid-solution alloys [56], implying that dislocation climb governs the creep mechanism for the diffusion weldment. The absolute inverse values of the slope of the double-logarithmic plot for the time to 1% creep strain

($|1/m_{1\%}|$) were in the range of 5.904–6.476. These values are slightly greater than those for the time-to-rupture plot. This is thought to result from the formation of Al-rich oxides along the interface. The Al-rich oxides can act as pinning obstacles at early creep stages with high efficiency; however, the Al-rich oxides become aligned at intervals of ~ 1.60 mm (the thickness of the sheet for diffusion welding). As the Al-rich oxides at the interfaces account for only a small fraction of the total amount, the overall creep mechanism at the early creep stages continues to be dislocation climb.

Table 3. The intercept and slope in the power-law function (Equation (1)).

Temperature (°C)	Time to Rupture		
	Intercept (A_{rup} , MPa·h ^{−m})	Slope (m_{rup})	$ 1/m_{rup} $
800	307.70	−0.193	5.172
850	215.12	−0.203	4.928
900	153.67	−0.215	4.639
950	92.46	−0.198	5.038
Temperature (°C)	Time to 1% Creep Strain		
	Intercept ($A_{1\%}$, MPa·h ^{−m})	Slope ($m_{1\%}$)	$ 1/m_{1\%} $
800	240.68	−0.169	5.904
850	–	–	–
900	83.10	−0.166	6.040
950	57.18	−0.154	6.476

3.3. Fractography

All specimens failed at an interface because the oxide-containing interfaces were much harder and less ductile than that of the matrix. Figure 6 shows the representative SEM morphology of the crept specimens, where Figure 6a,b show the fracture surfaces tested under 25 and 50 MPa at 900 °C, respectively. Necking at the interface is rarely observed without significant plastic deformation, regardless of the stress levels. Furthermore, the fracture surfaces are rather flat and perpendicular to the loading direction. The flat zone shows traces of mechanical grinding, which was performed during the surface preparation step for the diffusion-welding process. This is another indication of insufficient grain-boundary movement during the diffusion welding and post-weld heat treatment.

At higher magnification, two types of fracture morphologies were observed in the micrographs. They are classified into a brittle zone (denoted by B in blue) and ductile zone (denoted by D in yellow). The brittle zone occupies most of the fracture surface. Nonetheless, in the ductile zone, clear evidence of plastic deformation during the stress-rupture test is observed. Predominantly brittle fracture surfaces were previously reported for diffusion weldments. For example, Mylavaram et al. reported the immediate failure of applying a load to diffusion weldment [1]; they reported brittle failure with a flat surface, even with the aid of a Ni-foil interlayer between Alloy 617 plates.

3.4. Life Estimation

The Larson–Miller parameter is a time-temperature parameter (TTP) that has been widely used to predict long-term creep life (or stress) from short-term stress-rupture test data [57]. The Larson–Miller relation is expressed as follows:

$$LMP = T \cdot (\log(t) + C), \quad (2)$$

where LMP is the Larson–Miller parameter calculated from Equation (2); T is the temperature in kelvin; t is the time to rupture, time to the tertiary creep stage, or time to 1% creep strain in h depending on the purpose of the life estimation; C is a material constant. As pointed out by many researchers [58–60], determining C is critical in life estimation. A unique C value of 16.73 was used for estimating LMP (t_{rup}) following data analysis of creep

and creep-rupture at Idaho National Laboratory [60]. The same value was adopted for predicting LMP ($t_{1\%}$).

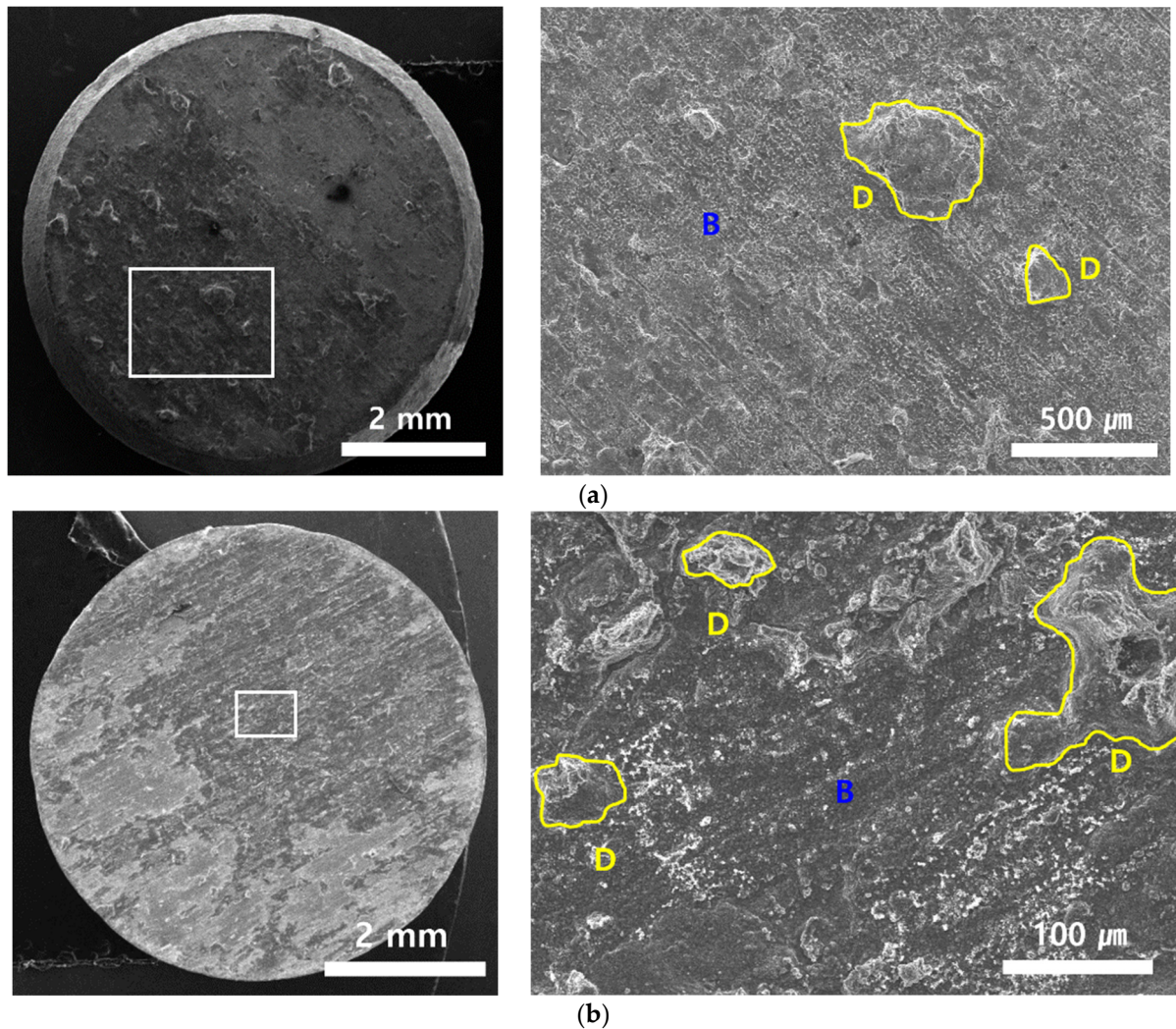


Figure 6. The representative fracture surface of the crept specimens. Stress-rupture tests were conducted at (a) 900 °C/25 MPa and (b) 900 °C/50 MPa.

LMP is also expressed as a linear function of stress:

$$LMP = f(\sigma) = B + n \cdot \log(\sigma), \quad (3)$$

where B is the intercept, and n is the slope of the plot of log stress versus LMP (t_{rup} and $t_{1\%}$).

Figure 7 shows the Larson–Miller relation of the diffusion weldment, where Figure 7a,b plot log stress versus LMP (t_{rup} and $t_{1\%}$, respectively). Data points and the corresponding regression for the as-received alloy are drawn for comparison. The data points for the as-received alloy were gathered from the authors' previous reports [61–63]. Table 4 lists the intercepts and slopes of both the as-received and diffusion-welded alloys.

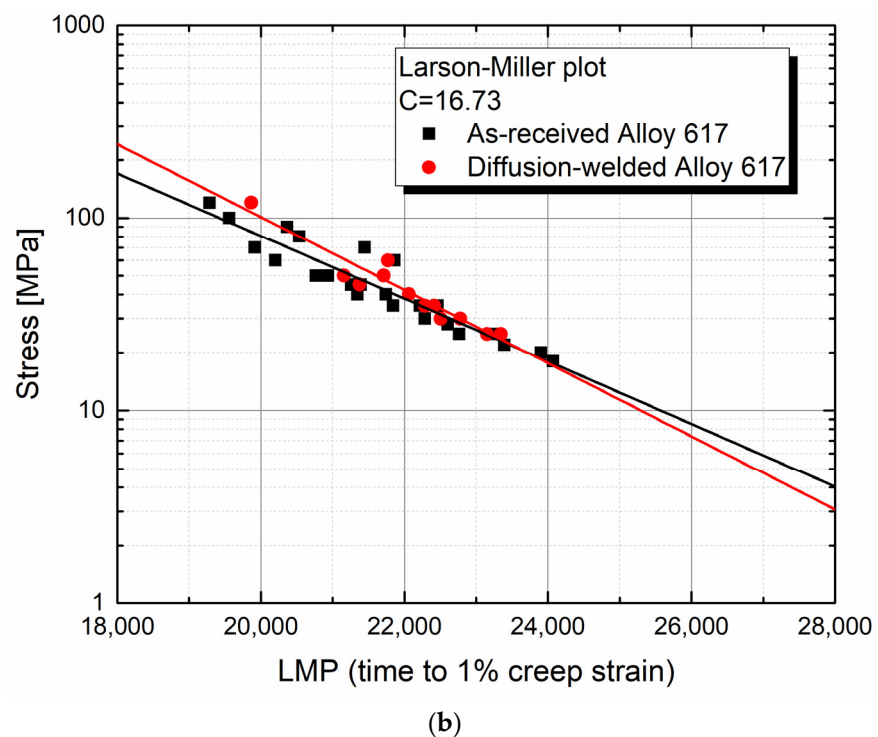
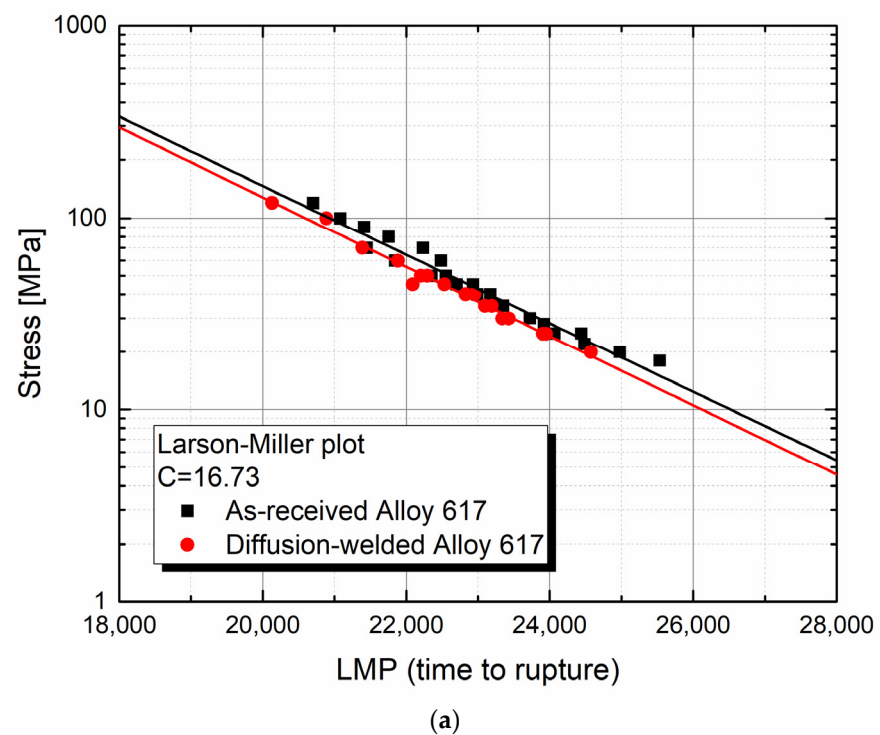


Figure 7. The plot of log stress versus *LMP* of the diffusion-welded Alloy 617. *LMP* is drawn for (a) the time to rupture and (b) the time to 1% creep strain. *LMP* of the as-received Alloy 617 (black square and black line) is drawn for comparison. Data of the as-received Alloy 617 were collected from Refs. [61–63].

Table 4. The intercept and the slope in the Larson–Miller relation (Equation (3)). C in Equation (2) is fixed to 16.73 for both the time to rupture and the time to 1% creep strain.

Alloy	Time to Rupture		
	Intercept (B_{rup})	Slope (n_{rup})	R^2
As-received	557,109	0.9995881	0.96620
Diffusion-welded	532,562	0.9995835	0.99268
Alloy	Time to 1% Creep Strain		
	Intercept ($B_{1\%}$)	Slope ($n_{1\%}$)	R^2
As-received	143,516	0.9996258	0.88747
Diffusion-welded	628,072	0.9995605	0.91368

For $LMP(t_{rup})$, the intercepts (B_{rup}) are 557,109 and 532,562 for the as-received and diffusion-welded Alloy 617, respectively. The intercept for the diffusion weldment reached ~95.59% of that for the as-received alloy, and similar observations were made for the slopes (n_{rup}) of the as-received and diffusion-welded alloys, implying that both alloys have the same creep deformation and fracture mechanism.

In contrast, $LMP(t_{1\%})$ shows anomalous behavior. The intercepts ($B_{1\%}$) were 143,516 and 628,072 for the as-received and diffusion-welded alloy, respectively. The intercept of the diffusion weldment was much higher than the practically achievable limit; moreover, the slope ($n_{1\%}$) of the diffusion weldment was lower than that of the as-received alloy. In other words, two straight lines intersect at an $LMP(t_{1\%})$ value of 23,347 and a stress value of 23.01 MPa (Figure 7b). This implies that in the low- $LMP(t_{1\%})$ range, the diffusion weldment requires higher stress than the as-received alloy to induce 1% creep strain, whereas the situation is the opposite in the high- $LMP(t_{1\%})$ range. Such phenomena seem to result from the presence of Al-rich oxides at the interfaces. As discussed above, Al-rich oxides placed in rows perpendicular to the loading direction can significantly obstruct creep deformation during the early creep stages. However, when the creep specimen enters the secondary creep stage, the oxide-containing interfaces cannot extend significantly. Therefore, in the high- $LMP(t_{1\%})$ range, stress values much lower than expected are inevitable for the diffusion weldment.

4. Conclusions

Diffusion welding with Alloy 617 was investigated for application to compact heat exchangers in the next-generation nuclear industry. The following conclusions can be drawn from the microscopic analysis and experimental stress-rupture tests.

(1) Al-rich oxides formed along the interface are strongly associated with planar grain boundaries at the interface. Such secondary precipitates inhibit the grain-boundary movement across the interface with high efficiency.

(2) The diffusion weldment showed limited creep strains (<9%) at high temperatures and crept specimens exhibited premature rupture at the interface. A ductile zone was partially observed, but a brittle zone occupied most of the fracture surface.

(3) The stress exponents obtained from double-logarithmic plots of log stress versus log time to rupture and log stress versus log time to 1% creep strain follow a power-law relation. An absolute inverse of the slope of ~5 in the plots indicates that dislocation climb is the dominant creep mechanism in the diffusion weldment.

(4) For $LMP(t_{rup})$, the intercept value of the diffusion weldment reached ~95.59% of that of the as-received alloy; a similar trend was observed for the slope. In contrast, $LMP(t_{1\%})$ showed anomalous behavior. For $LMP(t_{1\%})$ less than 23,347, the stress level of the diffusion weldment was higher than that of the as-received alloy, whereas, for $LMP(t_{1\%})$ greater than 23,347, the opposite was the case.

Author Contributions: Conceptualization, I.S. and E.-S.K.; methodology, I.S. and E.-S.K.; formal analysis, J.-B.H.; investigation, J.-B.H.; data curation, I.S.; writing—original draft preparation, I.S.; writing—review and editing, I.S.; visualization, I.S.; supervision, E.-S.K.; project administration, E.-S.K.; funding acquisition, E.-S.K. All authors have read and agreed to the published version of the manuscript.

Funding: This research was supported by a grant from the Nuclear Research and Development Program of the National Research Foundation of Korea (NRF) funded by the Ministry of Science, ICT and Future Planning (2016M2A8A1952772 and 2020M2D4A2068407).

Institutional Review Board Statement: Not applicable.

Informed Consent Statement: Not applicable.

Conflicts of Interest: The authors declare no conflict of interest.

References

1. Mylavarapu, S.K.; Sun, X.; Christensen, R.N.; Unocic, R.R.; Glosup, R.E.; Patterson, M.W. Fabrication and design aspects of high-temperature compact diffusion bonded heat exchangers. *Nucl. Eng. Des.* **2012**, *249*, 49–56. [\[CrossRef\]](#)
2. Mizokami, Y.; Igari, T.; Kawashima, F.; Sakakibara, N.; Tanihira, M.; Yuhara, T.; Hiroe, T. Development of structural design procedure of plate-fin heat exchangers for HTGR. *Nucl. Eng. Des.* **2013**, *255*, 248–262. [\[CrossRef\]](#)
3. Saranam, V.R.; Paul, B.K. Feasibility of using diffusion bonding for producing hybrid printed circuit heat exchangers for nuclear energy applications. *Procedia Manuf.* **2018**, *26*, 560–569. [\[CrossRef\]](#)
4. Ojo, O.A.; Richards, N.L.; Charturvedi, M.C. Effect of gap size and process parameters on diffusion brazing of Inconel 738. *Sci. Technol. Weld. Join.* **2004**, *9*, 209–220. [\[CrossRef\]](#)
5. Lukin, V.I.; Ryl'nikov, V.S.; Afanasyev-Khodykin, A.N. A nickel-based brazing alloy for brazing creep-resisting alloys and steels. *Weld. Int.* **2014**, *67*, 36–42. [\[CrossRef\]](#)
6. Riggs, B.; Alexandrov, B.; Benatar, A.; Xu, R. Metallurgical characterisations of CMSX-4 vacuum-brazed with BNi-2 and BNi-9. *Sci. Technol. Weld. Join.* **2017**, *22*, 227–235. [\[CrossRef\]](#)
7. Luo, Y.; Zhang, Q.; Jiang, W.; Zhang, Y.; Hao, M.; Tu, S.-T. The microstructure, mechanical properties and fracture behavior of hastelloy C276-BNi2 brazed joint. *Mater. Des.* **2017**, *115*, 458–466. [\[CrossRef\]](#)
8. Ghasemi, A.; Pouranvari, M. Microstructural evolution mechanism during brazing of Hastelloy X superalloy using Ni-Si-B filler metal. *Sci. Technol. Weld. Join.* **2018**, *23*, 441–448. [\[CrossRef\]](#)
9. Pouranvari, M.; Ekrami, A.; Kokabi, H. Role of base-metal composition in isothermal solidification during diffusion brazing of nickel-based superalloys. *Sci. Technol. Weld. Join.* **2018**, *23*, 13–18. [\[CrossRef\]](#)
10. Ghasemi, A.; Pouranvari, M. Intermetallic phase formation during brazing of a nickel alloy using a Ni-Cr-Si-Fe-B quinary filler alloy. *Sci. Technol. Weld. Join.* **2019**, *24*, 342–351. [\[CrossRef\]](#)
11. Gale, W.F.; Butts, D.A. Transient liquid phase bonding. *Sci. Technol. Weld. Join.* **2004**, *9*, 283–300. [\[CrossRef\]](#)
12. Jalilian, F.; Jahazi, M.; Drew, R.A.L. Microstructural evolution during transient liquid phase bonding of Inconel 617 using Ni-Si-B filler metal. *Mater. Sci. Eng. A* **2006**, *423*, 269–281. [\[CrossRef\]](#)
13. Arfafin, M.A.; Medraj, M.; Turner, D.P.; Bocher, P. Transient liquid phase bonding of Inconel 718 and Inconel 625 with BNi-2: Modeling and experimental investigations. *Mater. Sci. Eng. A* **2007**, *447*, 125–133. [\[CrossRef\]](#)
14. Ekrami, A.; Moeinifar, S.; Kokabi, A.H. Effect of transient liquid phase diffusion bonding on microstructure and properties of a nickel base superalloy Rene 80. *Mater. Sci. Eng. A* **2007**, *456*, 93–98. [\[CrossRef\]](#)
15. Tokoro, K.; Wikstrom, N.P.; Ojo, O.A.; Chaturvedi, M.C. Variation in diffusion-induced solidification rate of liquated Ni-Cr-B insert during TLP bonding of Waspalloy superalloy. *Mater. Sci. Eng. A* **2008**, *477*, 311–318. [\[CrossRef\]](#)
16. Ghoneim, A.; Ojo, O.A. Microstructure and mechanical response of transient liquid phase joint in Haynes 282 superalloy. *Mater. Charact.* **2011**, *62*, 1–7. [\[CrossRef\]](#)
17. Pouranvari, M. TLP bonding of a gamma prime strengthened superalloy using Ni-Si-B interlayer at 1150 °C-Part I: Microstructure. *World Appl. Sci. J.* **2011**, *15*, 1532–1536. Available online: [https://www.idosi.org/wasj/wasj15\(11\)11/8.pdf](https://www.idosi.org/wasj/wasj15(11)11/8.pdf) (accessed on 1 November 2011).
18. Pouranvari, M. TLP bonding of a gamma prime strengthened superalloy using Ni-Si-B interlayer at 1150 °C-Part II: Mechanical properties. *World Appl. Sci. J.* **2011**, *15*, 1507–1511. Available online: [https://www.idosi.org/wasj/wasj15\(11\)11/3.pdf](https://www.idosi.org/wasj/wasj15(11)11/3.pdf) (accessed on 1 November 2011).
19. Jalilian, F.; Jahazi, M.; Drew, R.A.L. Microstructure evolution during transient liquid phase bonding of alloy 617. *Metallurg Microstruct Anal.* **2013**, *2*, 170–182. [\[CrossRef\]](#)
20. Yang, Y.H.; Xie, Y.J.; Wang, M.S.; Ye, W. Microstructure and tensile properties of nickel-based superalloy K417G bonded using transient liquid-phase infiltration. *Mater. Des.* **2013**, *51*, 141–147. [\[CrossRef\]](#)
21. Pouranvari, M.; Ekrami, A.; Kokabi, A.H. TLP bonding of cast IN718 nickel based superalloy: Process-microstructure-strength characteristics. *Mater. Sci. Eng. A* **2013**, *568*, 76–82. [\[CrossRef\]](#)

22. Pouranvari, M.; Ekrami, A.; Kokabi, A.H. Transient liquid phase bonding of wrought IN718 nickel based superalloy using standard heat treatment cycles: Microstructure and mechanical properties. *Mater. Des.* **2013**, *50*, 694–701. [CrossRef]
23. Pouranvari, M. Solid solution strengthening of transient liquid phase bonded nickel based superalloy. *Mater. Sci. Technol.* **2015**, *31*, 1773–1780. [CrossRef]
24. Shakerin, S.; Omidvar, H.; Mirsalehi, S.E. The effect of substrate's heat treatment on microstructural and mechanical evolution of transient liquid phase bonded IN-738 LC. *Mater. Des.* **2016**, *89*, 611–619. [CrossRef]
25. Binesh, B.; Gharehbagh, A.J. Transient liquid phase bonding of IN738LC/MBF-15/IN738LC: Solidification behavior and mechanical properties. *J. Mater. Sci. Technol.* **2016**, *32*, 1137–1151. [CrossRef]
26. Pouranvari, M.; Ekrami, A.; Kokabi, A.H. Microstructure evolution mechanism during post-bond heat treatment of transient liquid phase bonded wrought IN718 superalloy: An approach to fabricate boride-free joints. *J. Alloys Compd.* **2017**, *723*, 84–91. [CrossRef]
27. Kapoor, M.; Doğan, Ö.N.; Carney, C.S.; Saranam, R.V.; Mcneff, P.; Paul, B.K. Transient-liquid-phase bonding of H230 Ni-based alloy using Ni-P interlayer: Microstructure and mechanical properties. *Metall. Mater. Trans. A* **2017**, *48*, 3343–3356. [CrossRef]
28. Esmaeili, H.; Mirsalehi, S.E.; Farzadi, A. Vacuum TLP bonding of Inconel 617 superalloy using Ni-Cr-Si-Fe-B filler metal: Metallurgical structure and mechanical properties. *Vacuum* **2018**, *152*, 305–311. [CrossRef]
29. Farzadi, A.; Esmaeili, H.; Mirsalehi, S.E. Transient liquid phase bonding of Inconel 617 superalloy: Effect of filler metal type and bonding time. *Weld. World* **2019**, *63*, 191–200. [CrossRef]
30. Zhang, G.; Chandel, R.S.; Seow, H.P. Solid state diffusion bonding of Inconel 718. *Sci. Technol. Weld. Join.* **2001**, *6*, 235–239. [CrossRef]
31. Shizadi, A.A.; Wallach, E.R. New method to diffusion bond superalloys. *Sci. Technol. Weld. Join.* **2004**, *9*, 37–40. [CrossRef]
32. Totemeier, T.C.; Tian, H.; Clark, D.E.; Simpson, J.A. Microstructure and Strength Characteristics of Alloy 617 Welds. Idaho National Laboratory **2005**, INL/EXT-05-00488. Available online: <https://core.ac.uk/download/pdf/71313108.pdf> (accessed on 1 June 2005).
33. Ravisankar, B.; Krishnamoorthi, J.; Ramakrishnan, S.S.; Angelo, P.C. Diffusion bonding of SU 263. *J. Mater. Process. Technol.* **2009**, *209*, 2135–2144. [CrossRef]
34. Basuki, W.W.; Kraft, O.; Aktaa, J. Optimization of solid-state diffusion bonding of Hastelloy C-22 for micro heat exchanger applications by coupling of experiments and simulations. *Mater. Sci. Eng. A* **2015**, *538*, 340–348. [CrossRef]
35. Mizia, R.E.; Clark, D.E.; Glazoff, M.W.; Lister, T.E.; Trowbridge, T.L. Optimizing the diffusion welding process for Alloy 800H: Thermodynamic, diffusion modeling, and experimental work. *Metall. Mater. Trans. A* **2013**, *44*, 154–161. [CrossRef]
36. Sah, I.; Kim, D.; Lee, H.J.; Jang, C. The recovery of tensile ductility in diffusion-bonded Ni-base alloys by post-bond heat treatments. *Mater. Des.* **2013**, *47*, 581–589. [CrossRef]
37. Song, C.H.; Cho, I.H.; Choi, J.S. A study on diffusion bonding performance of Inconel 617 heat exchanger. *Int. J. Precis. Eng. Manuf.* **2015**, *16*, 957–963. [CrossRef]
38. Xiong, J.; Peng, Y.; Samiuddin, M.; Yuan, L.; Li, J. Common mechanical properties of diffusion bonded joints and their corresponding microstructure features. *J. Mater. Eng. Perform.* **2020**, *29*, 3277–3286. [CrossRef]
39. Sah, I.; Hwang, J.-B.; Kim, W.-G.; Kim, E.-S.; Kim, M.-H. High-temperature mechanical behaviors of diffusion-welded Alloy 617. *Nucl. Eng. Des.* **2020**, *364*, 110617. [CrossRef]
40. Nestell, J.; Sham, T.-L. ASME Code Consideration for the Compact Heat Exchanger. Oak Ridge National Laboratory. 2015, ORNL/TM-2015/401. Available online: <https://info.ornl.gov/sites/publications/Files/Pub57987.pdf> (accessed on 31 August 2015).
41. Aakre, S.R.; Jentz, I.W.; Anderson, M.H. Nuclear Code Case Development of Printed-Circuit Heat Exchangers with Thermal and Mechanical Performance Testing. In Proceedings of the 6th International CO₂ Power Cycles Symposium, Pittsburgh, PA, USA, 27–29 March 2018. Available online: http://sco2symposium.com/papers2018/heat-exchangers/114_Paper.pdf (accessed on 27 March 2018).
42. Mahajan, H.P.; Jentz, I.; Hassan, T. Allowable stress development of diffusion bonded Alloy 800H for Section III. In *Pressure Vessels and Piping Conference*; American Society of Mechanical Engineers: New York, NY, USA, 2020. [CrossRef]
43. Keating, R.B.; McKillop, S.P.; Allen, T.; Anderson, M. ASME boiler and pressure vessel code roadmap for compact heat exchanger in high temperature reactors. *J. Nucl. Rad. Sci.* **2020**, *6*, 041106. [CrossRef]
44. Shi, D.; Dong, C.; Yang, X.; Zhang, L.; Hou, J.; Liu, Y. Experimental investigations on creep rupture strength and failure mechanism of vacuum brazed joints of a DS superalloy at elevated temperature. *Mater. Sci. Eng. A* **2012**, *545*, 162–167. [CrossRef]
45. Luo, Y.; Jiang, W.; Zhang, Y.; Hao, M.; Tu, S.-T. Creep rupture behavior of Hastelloy C276-BNi2 brazed joint. *Mater. Sci. Eng. A* **2018**, *711*, 223–232. [CrossRef]
46. Chai, L.; Huang, J.; Hou, J.; Lang, B.; Wang, L. Effect of holding time on microstructure and properties of transient liquid-base-bonded joints of a single crystal alloy. *J. Mater. Eng. Perform.* **2015**, *24*, 2287–2293. [CrossRef]
47. Rozman, K.A.; Carl, M.A.; Kapoor, M.; Doğan, Ö.N.; Hawk, J.A. Creep performance of transient liquid phase bonded Haynes 230 alloy. *Mater. Sci. Eng. A* **2019**, *768*, 138477. [CrossRef]
48. Asadi, J.; Sajjadi, S.A.; Omidvar, H. Creep properties of Ni-based superalloy GTD-111 joints produced by transient liquid phase method using BNi-3 filler. *J. Manuf. Process.* **2020**, *58*, 1103–1114. [CrossRef]

49. Malekan, A.; Farvizi, M.; Mirsalehi, S.E.; Saito, N.; Nakashima, K. Holding time influence on creep behavior of transient liquid phase bonded joints of Hastelloy X. *Mater. Sci. Eng. A* **2020**, *772*, 138694. [[CrossRef](#)]
50. Elliot, S.; Bucklow, I.A.; Wallach, E.R. An examination of diffusion bonded interfaces in a mild steel. *J. Mater. Sci* **1980**, *15*, 2823–2833. [[CrossRef](#)]
51. Takahashi, Y.; Nakamura, T.; Nishiguchi, K. Dissolution process of surface oxide film during diffusion bonding of metals. *J. Mater. Sci.* **1992**, *27*, 485–498. [[CrossRef](#)]
52. Ashworth, M.A.; Jacobs, M.H.; Davies, S. Basic mechanisms and interface reactions in HIP diffusion bonding. *Mater. Des.* **2000**, *21*, 351–358. [[CrossRef](#)]
53. Shirzadi, A.A.; Assadi, H.; Wallach, E.R. Interface evolution and bond strength when diffusion bonding materials with stable oxide films. *Surf. Interface Anal.* **2001**, *31*, 609–618. [[CrossRef](#)]
54. Cox, M.J.; Kim, M.J.; Carpenter, R.W. Interface nanochemistry effects on stainless steel diffusion bonding. *Metall. Mater. Trans. A* **2002**, *33*, 437–442. [[CrossRef](#)]
55. Penkalla, H.-J.; Over, H.-H.; Schubert, F. Constitutive equations for the description of creep and creep rupture behavior of metallic materials at temperatures above 800 °C. *Nucl. Technol.* **1984**, *66*, 685–692. [[CrossRef](#)]
56. Kassner, M.E. Five-Power-Law Creep. In *Fundamentals of Creep in Metals and Alloys*, 3rd ed.; Elsevier: Amsterdam, The Netherlands, 2015; pp. 7–102.
57. Larson, F.R.; Miller, J. A time-temperature relationship for rupture and creep stresses. *Trans. ASME* **1952**, *74*, 765–775.
58. Kim, W.-G.; Yin, S.-N.; Kim, Y.-W.; Ryu, W.-S. Creep behavior and long-term creep life extrapolation of alloy 617 for a very high temperature gas-cooled reactor. *Trans. Indian Inst. Met.* **2010**, *63*, 145–150. [[CrossRef](#)]
59. Kim, W.-G.; Yin, S.-N.; Lee, G.-G.; Kim, Y.-W.; Kim, S.-J. Creep oxidation behavior and creep strength prediction for Alloy 617. *Int. J. Press Vessel. Pip.* **2010**, *87*, 289–295. [[CrossRef](#)]
60. Wright, J.K.; Lillo, T.M.; Wright, R.N.; Kim, W.-G.; Sah, I.-S.; Kim, E.-S.; Park, J.-Y.; Kim, M.-H. Creep and creep-rupture of Alloy 617. *Nucl. Eng. Des.* **2018**, *329*, 142–146. [[CrossRef](#)]
61. Kim, W.-G.; Park, J.-Y.; Lee, G.-G.; Hong, S.-D.; Kim, Y.-W. Temperature effect on the creep behavior of alloy 617 in air and helium environments. *Nucl. Eng. Des.* **2014**, *271*, 291–300. [[CrossRef](#)]
62. Kim, W.-G.; Park, J.-Y.; Ekaputra, I.M.W.; Kim, S.-J.; Kim, M.-H.; Kim, Y.-W. Creep deformation and rupture behavior of Alloy 617. *Eng. Fail. Anal.* **2015**, *58*, 441–451. [[CrossRef](#)]
63. Kim, W.-G.; Ekaputra, I.M.W.; Park, J.-Y.; Kim, M.-H.; Kim, Y.-W. Investigation of creep rupture properties in air and He environments of alloy 617 at 800 °C. *Nucl. Eng. Des.* **2016**, *306*, 177–185. [[CrossRef](#)]